Chem

CellPress

Article

High-Throughput Multi-parametric Imaging Flow Cytometry

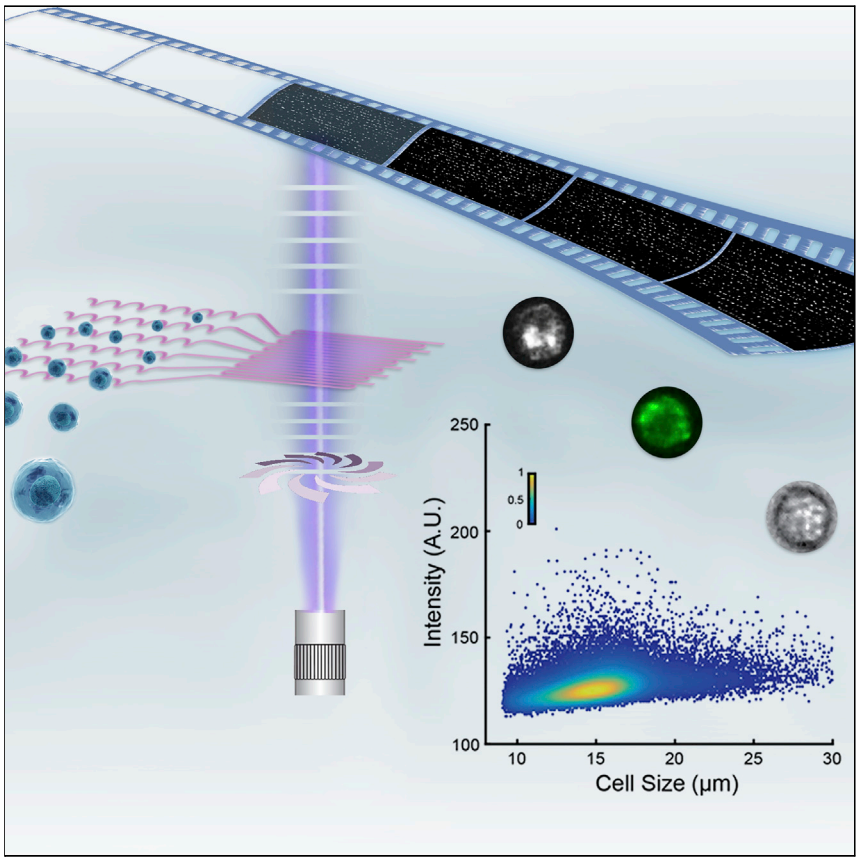

We present a sheathless, microfluidic imaging flow cytometer incorporating stroboscopic illumination for blur-free analysis of single cells at throughputs in excess of 50,000 cells/s. The imaging platform is capable of accurate sizing and multi-parametric quantification of both large and heterogeneous cell populations. We demonstrate the efficacy of the approach through the performance of ultra-high-throughput apoptosis detection and cell-cycle analysis. Such an imaging flow cytometry platform transforms the utility of traditional fluorescent cytometers through the addition of morphological information at high throughput, which will potentially allow for large-scale phenotypic characterization analysis.

Anandkumar S. Rane, Justina Rutkauskaite, Andrew deMello, Stavros Stavrakis

andrew.demello@chem.ethz.ch (A.dM.)
stavros.stavrakis@chem.ethz.ch (S.S.)

HIGHLIGHTS

An ultra-high-throughput (>50,000 cells/s) method for imaging flow cytometry

Multi-parametric (fluorescence, bright-field, and dark-field) imaging of single cells

Ultra-fast discrimination of cell-cycle phases in large cellular populations

Rapid, accurate, and sensitive analysis of apoptotic cells at the single-cell level

Rane et al., Chem 3, 588–602
October 12, 2017 © 2017 Elsevier Inc.
http://dx.doi.org/10.1016/j.chempr.2017.08.005

Chem

CellPress

Article

High-Throughput Multi-parametric Imaging Flow Cytometry

Anandkumar S. Rane,[1] Justina Rutkauskaite,[1] Andrew deMello,[1,2,*] and Stavros Stavrakis[1,*]

SUMMARY

Flow cytometry, incorporating either point- or imaging-based detection schemes, is recognized to be the gold-standard tool for high-throughput manipulation and analysis of single cells in flow but is typically limited in either the number of cells that can be interrogated per unit of time or the resolution with which individual cells can be imaged. To address these limitations, we present a sheathless, microfluidic imaging flow cytometer incorporating stroboscopic illumination for blur-free cellular analysis at throughputs exceeding 50,000 cells/s. By combining inertial focusing of cells in parallel microchannels and stroboscopic illumination, the chip-based cytometer is able to extract multi-color fluorescence, bright-field, and dark-field images and perform accurate sizing of individual cells and analysis of heterogeneous cell suspensions while maintaining operational simplicity. To showcase the efficacy of the approach, we apply the method to the rapid enumeration of apoptotic cells and the high-throughput discrimination of cell-cycle phases.

INTRODUCTION

Flow cytometry is widely recognized as the gold-standard technique for the rapid detection and enumeration of microscale cellular populations and represents a key tool in fields such as cancer diagnostics,[1] massively parallel DNA sequencing,[2] T cell phenotyping,[3] rare-cell detection,[4] and single-cell proteomics.[5] Contemporary flow cytometers are able to analyze several thousand cells (or particles) per second and can isolate cells according to precise scattering or fluorescence criteria. Nevertheless, although conventional fluorescence cytometers provide impressively efficient analysis of individual cells at high throughput, they are costly, mechanically complex, and require excessively large sample volumes and trained personnel for operation.[6] These features have unsurprisingly limited their use in many areas of biological and clinical research. To address these limitations, a number of microfabricated flow cytometers have been presented and have proved successful in assaying cellular populations at throughputs that are competitive with those achieved in conventional formats. That said, most of these microfluidic cytometers have focused on the direct transfer of macroscale components to planar chip formats,[6–8] and although they exhibit excellent detection sensitivities, analytical throughputs rarely exceed 2,000 cells/s and it is difficult to extract detailed information regarding cell size and morphology.

Imaging flow cytometry offers an entirely different approach to conventional flow cytometry, through the performance of rapid but high-resolution imaging of single cells within flowing environments, and contrasts with point-based (or serial) detection schemes used in most high-end commercial and microfluidic flow cytometers. Interestingly, the few reports of microfluidic imaging-based flow cytometers in the

The Bigger Picture

Imaging flow cytometry combines the high-throughput capabilities of conventional flow cytometry with single-cell imaging and represents the gold-standard method for information-rich analysis of cellular populations. Microfluidic flow cytometers have recently been shown to be powerful tools for the analysis of single cells in flow but typically exhibit sub-optimal throughput because of their reliance on single-point detection schemes. To address this limitation, we introduce sheathless, microfluidic imaging flow cytometry, a technique that incorporates stroboscopic illumination for blur-free detection at throughputs in excess of 50,000 cells/s. The imaging platform allows for the rapid and efficient extraction of multi-color fluorescence intensities, accurate sizing of mixed cell populations, and mapping of intracellular heterogeneities. This enables the accurate enumeration of apoptotic cells in a given sample and cell-cycle phase discrimination in an ultra-high-throughput manner.

CrossMark

literature have incorporated either exotic bright-field imaging detection schemes[9] or utilized massively parallel fluidics combined with high-speed imaging to image large numbers of cells per acquisition frame.[10,11] Significantly, the high-speed cameras required for such measurements can only be used for bright-field imaging because of their intrinsically low quantum efficiencies.[10,11] In this respect, label-free imaging modalities provide information primarily related to cellular size and morphology and lack the sensitivity, specificity, and information content of fluorescence-based approaches. An elegant approach to parallelization combined with confocal fluorescence imaging was introduced in 2011 by McKenna and co-workers for rare-cell detection; however, the relatively low-throughput of 10^3 cells/s and a lack of morphological and sizing information limits such an approach in real-world applications.[12] More recently, Diebold et al. reported a novel fluorescence imaging technique that accesses pixel readout rates significantly higher than conventional electron multiplier charge-coupled cameras (EMCCDs), thus enabling fluorescence imaging of human breast carcinoma cells moving at speeds of 1 m/s.[13] On the basis of the analysis of achievable flow rates, the authors extrapolated a hypothetical throughput of 50,000 cells/s. Although the authors were successful in achieving blur-free fluorescence imaging, the complexity of the optical detection system severely limits widespread adoption in non-expert laboratories. In addition, commercial imaging flow cytometers are now available offering high-resolution, multiplexed imaging but with maximum throughputs of approximately 4,000 cells/s.[14]

To address the aforementioned limitations, we describe a microfluidic fluorescence imaging flow cytometer that utilizes sheathless inertial focusing (to ensure high cellular occupancy within the field of view) and stroboscopic epifluorescence imaging[15] (to extract blur-free images at high linear flow velocities) to efficiently image and size cells at throughputs between 50,000 and 100,000 cells/s. Significantly, we show that the method can be applied to multi-parametric analysis of cellular populations through the use of bright-field and dark-field imaging (for size and morphology analysis) in addition to multi-color fluorescence detection. To demonstrate the utility of our approach, we apply the developed platform to high-throughput apoptosis detection and cell-cycle analysis.

RESULTS

A schematic of the microfluidic device is shown in Figures 1 and S1A. In basic terms, it consists of three sub-components: an input module (R1) incorporating a series of structures or posts to remove cellular aggregates and particulates prior to analysis, a cell-focusing manifold (R2) containing six parallel but winding channels (each with a width and depth of 40 and 22 μm, respectively), and an imaging region (R3) where dual-color fluorescence, bright-field, and dark-field images of the cell flows can be extracted. In addition to lateral focusing, fluid inertia provides control over the axial position of cells within the microfluidic channel and the inter-cellular spacings (see Figures S2 and S3).[16] To eliminate motion blur intrinsically associated with CMOS cameras when imaging rapidly moving cells, we implemented a stroboscopic illumination scheme and dual-view detection system, to extract blur-free images (see Figure S4). We have previously used such a strategy to good effect when performing high-throughput, quantitative enzyme kinetic analysis in segmented flows.[15]

To ensure maximal throughput, the volumetric flow rate of the input cell suspension is adjusted so that cells are not under- or oversampled during the imaging process. This is achieved by synchronizing the cell velocity with the rate of acquisition of the

[1]Institute for Chemical and Bioengineering, Department of Chemistry and Applied Biosciences, ETH Zürich, Vladimir Prelog Weg 1, Zürich 8093, Switzerland

[2]Lead Contact

*Correspondence: andrew.demello@chem.ethz.ch (A.dM.), stavros.stavrakis@chem.ethz.ch (S.S.)

http://dx.doi.org/10.1016/j.chempr.2017.08.005

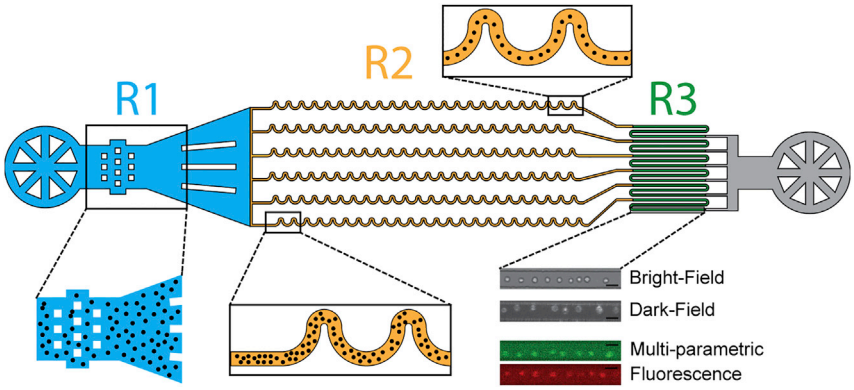

Figure 1. Microfluidic Flow Cytometer Design and Characterization

Schematic of the microfluidic flow cytometer with inlet port (blue), inertial focusing channels for the sheathless manipulation of the cells (orange), imaging area for the detection (green), and the outlet port for the collection (gray). (R1) Filter for removing the cell debris, cell aggregates, and the clumps. (R2) Schematic of the cells flowing at the beginning and at the end of the inertial focusing channel. (R3) Representative images from all the possible imaging modalities of the detection: bright-field imaging analogous to the forward-scatter measurements on a commercial flow cytometer for information on the size of the cells, dark-field imaging analogous to the side-scatter measurements on a commercial flow cytometer for the cell morphology, and the multi-parametric fluorescence imaging for cell phenotyping based on the fluorescence labeling. All scale bars represent 30 μm.

camera. Given that each microchannel forms three channels in the detection area, a total flow length of 4,005 μm per flow channel is realized. The image acquisition rate is set to 120 frames/s, and a new frame is captured every 8 ms. If a particular cell traverses the channel at a velocity appreciably lower than this rate of frame capture, it will be imaged more than once during the acquisition. Similarly, if a cell travels significantly faster than the frame acquisition rate, the cell can pass the detection region without being imaged. On the basis of these criteria (and for the current system), cells should traverse at a linear flow velocity of approximately 0.4 m/s. It has previously been shown that cells focused with fluid inertia move at a (constant) velocity approximately 0.8 times the maximum velocity in the channel.[17] In the current situation, this would correspond to an average volumetric flow rate of 25 μL/min in each of the flow channels and a total flow rate of 150 μL/min. Such conditions ensure that every cell that enters the field of view of the camera traverses the entire length of the channel and is outside the detection zone by the next frame. Crucially, the number of cells detected in each frame is maximized by working at concentrations high enough to allow axial packing at compact spacings.[18]

To evaluate whether our microfluidic platform can serve as an effective flow cytometer, 10 μm fluorescent polystyrene particles were injected at a flow rate of 30 μL/min, inertially focused, and imaged with a stroboscopic epifluorescence excitation of 10 μs duration at 120 fps (Figure 2A, inset). Operating at a particle concentration of 20 million/mL, acquisition is accomplished in 6.5 min and corresponds to the analysis of 5×10^4 particles/s. To quantify the accuracy and reproducibility of the microfluidic platform, the coefficient of variation (CV) of pulse height distributions were extracted and analyzed. Fluorescence histograms show a single distribution (Figure 2A) with a mean diameter of 9.95 μm and a standard deviation (SD) of 0.62 μm. This is in excellent agreement with data provided by the vendor (mean diameter of 9.94 μm and SD of 0.76 μm). Figure 2B reports the variation of fluorescence intensity with size for the bead population. Subsequently, the efficiency of the device in extracting population characteristics when assaying heterogeneous

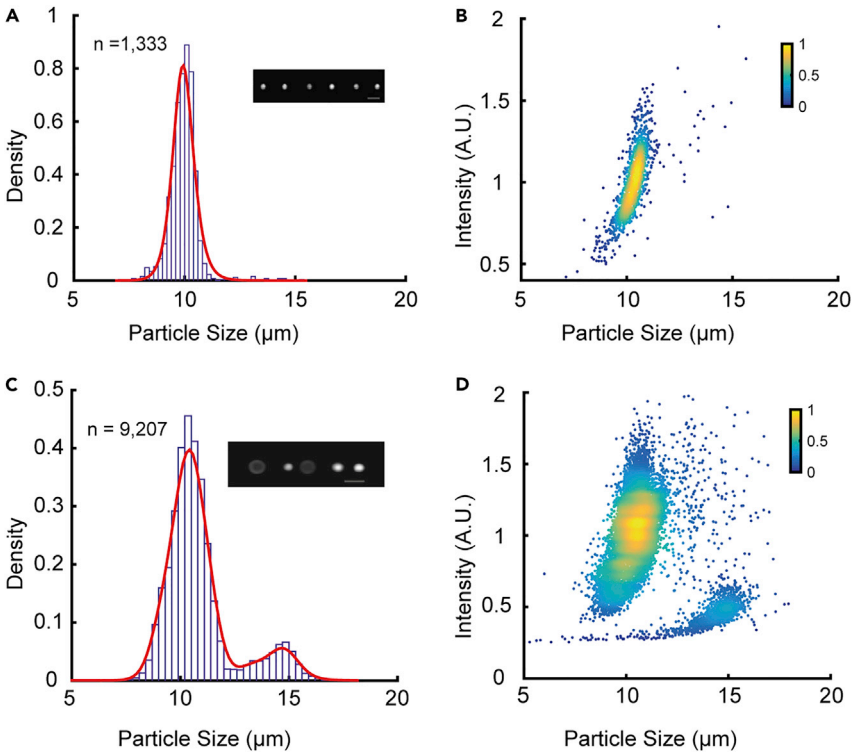

Figure 2. High-Throughput Microparticle Analysis via Microfluidic Flow Cytometry

(A and B) Size histogram (A) and variation of fluorescence intensity as a function of size (B) for a population of 10 μm fluorescent beads (inset: image of beads flowing at 0.4 m/s).

(C and D) Size histogram (C) and variation of fluorescence intensity as a function of size (D) for a mixture of 10 μm and 15 μm fluorescent beads (inset: image of beads flowing at 30 μL/min).

All scale bars represent 20 μm.

particle populations was assessed with a sample consisting of 10 μm and 15 μm polystyrene particles with different integrated fluorescence intensities. Fluorescence images of the particles were analyzed (see Experimental Procedures) and the extracted histogram is shown in Figure 2C. Again, data are in excellent agreement with vendor specifications for each individual population (see Table S1). Inspection of the scatterplot of fluorescence intensity versus particle size demonstrates that detection events can be grouped into two distinct regions (Figure 2D), confirming that the system can robustly identify each individual sub-population. The 10 μm fluorescent beads have an intrinsically higher fluorescence intensity than the 15 μm fluorescent beads. This is confirmed both from the scatterplot and also from images of the fluorescent beads in flow (Figure 2C, inset).

To further demonstrate the accuracy of fluorescence intensity quantitation, we measured the CV of the mean fluorescence intensity of the population (see Figures S5A and S5B). The intensity CV is approximately three times the size CV, which is as expected for internally labeled particles because dye labeling scales with the volume. Importantly, the extracted size and fluorescence intensity is in accordance with the vendor's specifications, demonstrating the robustness of inertial focusing, because variations in size are highly sensitive to particle position within the microchannel, even with high-magnification and high-numerical-aperture (NA) objectives (see Figures S5C and S5D). Moreover, the imaging approach allows quantification of heterogeneity in the uptake of the fluorescent dye within individual

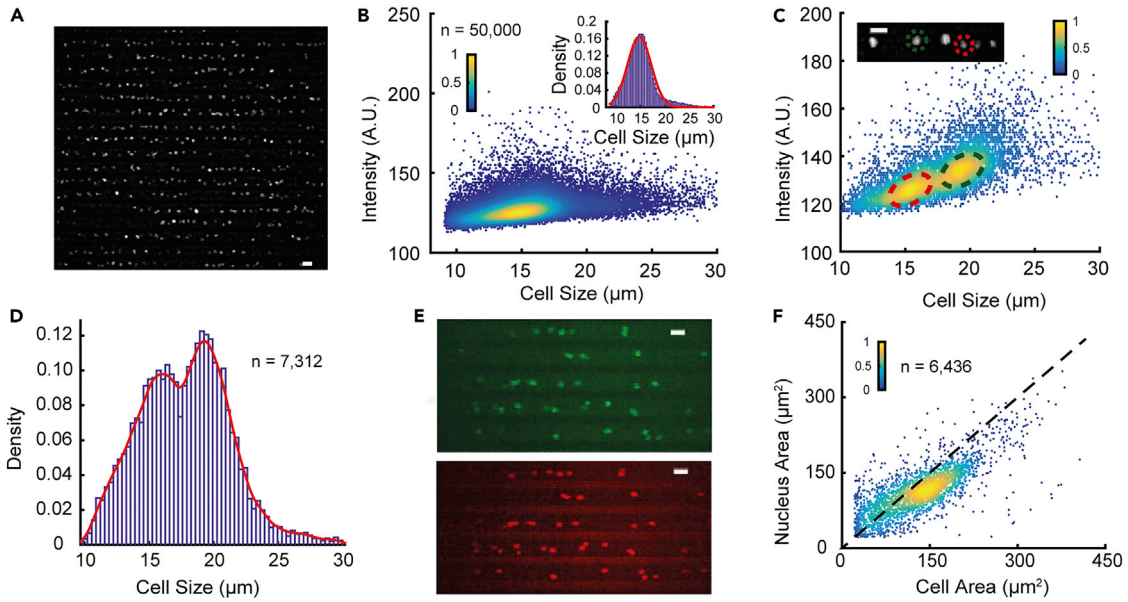

Figure 3. High-Throughput and Multi-parametric Detection

(A) A grayscale image of the HL60 cells flowing in the parallel flow cytometry microdevice at an average flow velocity of 0.35 m/s was captured with a stroboscopic duration of 10 μs.

(B) Scatterplot reporting fluorescence intensity versus cell size for HL60 cells (inset: size histogram for the HL60 cells).

(C and D) Scatterplot (C) and size histogram (D) showing discrete populations in a 1:1 mixture of HL60 cells and K562 cells (inset in C: images of HL60 cells [circled in green] and K562 cells [circled in red]).

(E) A false-color image of HL60 cells labeled with membrane dye Alexa WGA (green) and the nuclear stain DRAQ5 (red) at a flow velocity of 0.35 m/s was captured with a stroboscopic duration of 10 μs.

(F) Scatterplot of nuclear area against the cellular area for the HL60 cell population measured from each of the detection channels.

All scale bars represent 40 μm.

particles and variations between different bead populations (see Figures S5E and S5F). The CV is primarily controlled by intrinsic variations in the fluorophore concentration and size of the particles but is also dependent on the axial position of the particle within the microchannel, with any axial deviations resulting in a reduction in the emission intensity. Significantly, the CVs obtained from the histograms are well within the acceptable limits for resolving population characteristics according to fluorescence intensities and size. Accordingly, to quantify the dynamic range and detection efficiency of the imaging platform, we assayed five bead populations moving at an average linear velocity of 0.35 m/s. Inspection of Figure S6 confirms the uniformity of the image intensities and demonstrates the efficiency of inertial focusing.

Subsequently, we performed high-throughput single-cell analysis by utilizing the full field of view of the CMOS sensor (2,048 × 2,048 pixels) and the parallel microchannel network (Figure 3A). Analysis of a high-concentration HL60 cell suspension (40 × 10^6 cells/mL) was achieved at a throughput of 50,000 cells/s (450 cells/frame; Figure 3B, inset) and yielded a mean cell diameter of 15.5 μm and CV of 17.8% for a population of 49,057 cells (Figure 3B). Crucially, pulse durations of 10 μs yield a negligible blur of 0.15 μm in the mean cell diameter in comparison with the measurements from static images (see Figure S7 and Supplemental Experimental Procedures, Supplemental Note 1). Furthermore, the CV of fluorescence intensity is similar to that obtained from static images (see Figure S8 and Supplemental Experimental Procedures, Supplemental Note 2). As noted, the platform is ideal for applications that require analysis of labeling heterogeneities inside cells as can been seen in Figures S9A and S9B. Assuming a uniform spacing between

cells of 25 μm and a cell diameter of 15 μm, then on the basis of achievable frame rates, the imaging cytometer provides for a maximum throughput of approximately 96,000 cells/s (see Supplemental Experimental Procedures, Supplemental Note 3). The exceptionally high throughput of the microfluidic device is engendered by the self-assembly of cells in the detection region (mediated by upstream inertial focusing) and the camera sensor size. By synchronizing the flow rate of the sample with the acquisition rate of the camera, oversampling or undersampling of the cell population is always avoided.

Perhaps the most powerful feature of the described platform is the ability to efficiently analyze multiple cell populations in high throughput. The variation of fluorescence intensity as a function of cell size (Figure 3C) demonstrates the ability to accurately determine the distribution of two cell lines with size diameters of 14.8 μm and 19.6 μm in a 1:1 mixture of HL60 and K562 cells (see Figures 3D and S10, and Table S2). To further demonstrate the precision of the focusing and imaging system for quantitative analysis of multi-color measurements, we adopted a dual-color optics configuration and evaluated the sub-cellular localization of nuclei in fast-flowing HL60 cells (Figure 3E) to extract both cell and nucleus size (Figure 3F). The nucleus-to-cytoplasmic ratios obtained from measurements in flow and from static images are in excellent agreement (see Figure S11 and Supplemental Experimental Procedures, Supplemental Note 4). This parameter is commonly used in the determination of cell maturity during the cell cycle.[19] The dual-view optics configuration also allows the implementation of a bright-field imaging modality for the concurrent investigation of cell size and morphology (see Figure S12).

Subsequently, we used the microfluidic cytometer to perform high-throughput cell-cycle analysis, with the aim of distinguishing cell-cycle phases of an HL60 cell population. Contour plots of nuclear area versus fluorescence intensity (Figure 4A) associated with each of the cell phases report clear differences between G1 and G2 synchronized populations, with each sub-population being accurately quantified via dark-field and fluorescence intensity measurements (Figure 4C). Control measurements obtained from a commercial flow cytometer confirm these observations (Figures 4B and 4D). Importantly, to concurrently probe nucleus size and cell morphology, we also performed simultaneous fluorescence and dark-field imaging (Figure 4E), with dark-field imaging data providing a direct measure of cell size (Figure 4F). As expected, the imaging cytometer is able to resolve the difference in size between cells in the G1 and G2 phases (as a result of an increase in nuclear content), given that sub-population overlap is significantly lower than with forward-scatter analyses using commercial flow cytometry (Figures 4F and 4G).[20] Furthermore, we were able to directly evaluate nuclear size through fluorescence imaging (Figure 4H), which to the best of our knowledge cannot be extracted with commercial flow cytometry platforms. Finally, imaging enables the facile elimination of false-positive events, such as G1 doublets, which would be detected as "G2 positives" in conventional flow cytometers (see Figure S13 and Supplemental Experimental Procedures, Supplemental Note 5).

Finally, there is much current interest in studying cells undergoing programmed self-destruction via apoptosis.[21] To address this problem, we labeled Jurkat cells with the fluorogenic substrate caspase-3/-7 (a marker of caspase activation in the apoptotic cells) and propidium iodide for detecting cell-membrane permeability. To enhance sensitivity for high-throughput analysis, we shaped the laser beam to a light sheet, modified the flow conditions (see Experimental Procedures

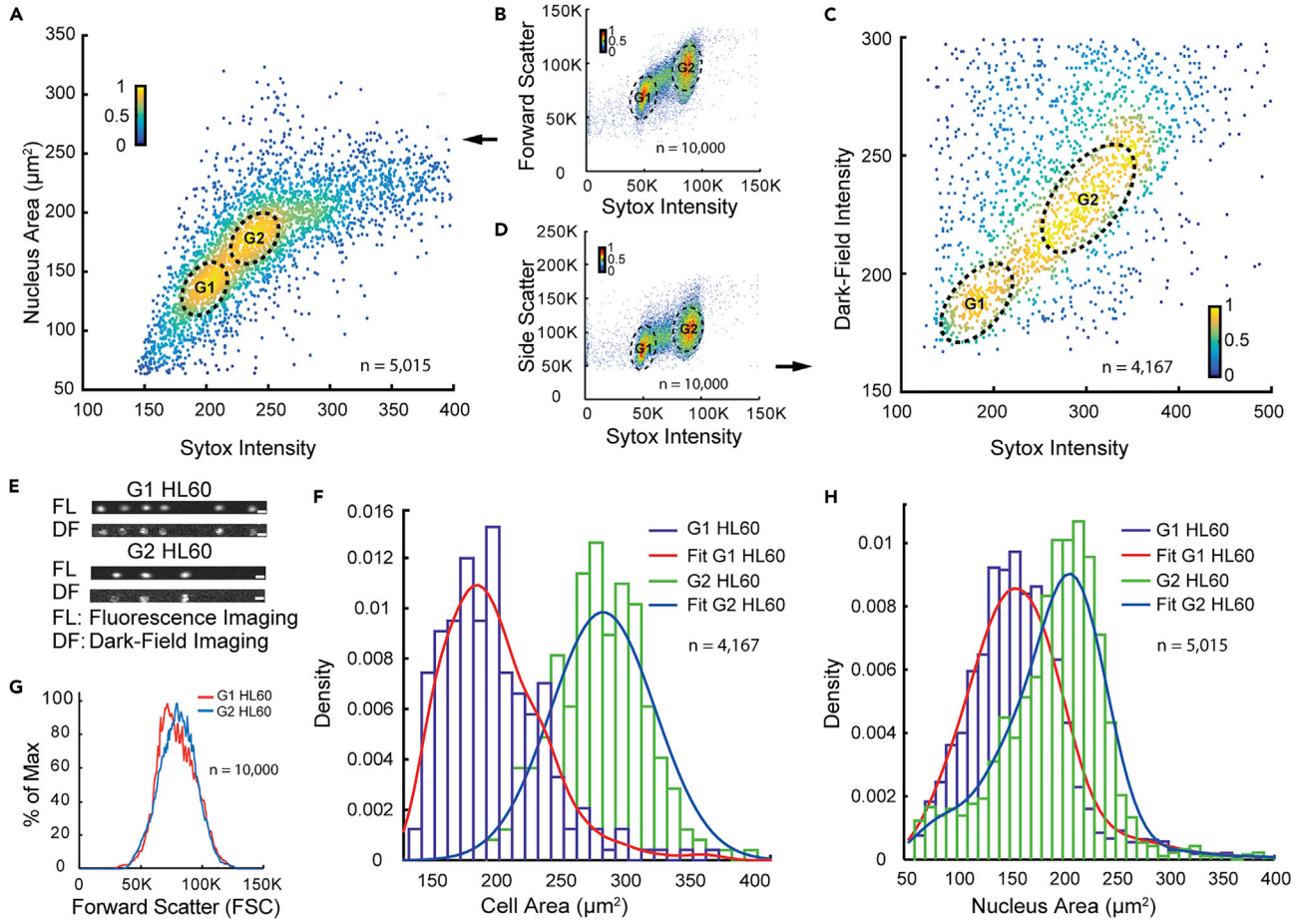

Figure 4. Cell-Cycle Analysis Using Microfluidic Flow Cytometry

(A) Scatterplot of nucleus area against fluorescence intensity for G1 and G2 synchronized HL60 cell populations.

(B) Variation of forward scatter as a function of fluorescence intensity measured with a commercial flow cytometer.

(C) Scatterplot of dark-field intensity against fluorescence intensity for G1 and G2 synchronized HL60 cell populations.

(D) Scatterplot of side scatter versus fluorescence intensity obtained from a commercial flow cytometer.

(E) Representative fluorescence and dark-field images for G1 and G2 synchronized HL60 populations moving at a flow velocity of 0.35 m/s.

(F) Cell-area histogram for G1 and G2 synchronized HL60 cell populations constructed from dark-field imaging data.

(G) Forward-scatter histogram for G1 and G2 synchronized HL60 cell populations obtained from commercial flow cytometric measurements.

(H) Nuclear area histogram for G1 and G2 synchronized HL60 cell populations extracted from fluorescence imaging data.

All scale bars represent 20 μm.

and Figure S14), and implemented a dual-color detection configuration. Figure 5A displays representative images of early and late apoptotic Jurkat cells. Cells exhibiting weak fluorescence are alive (dashed red circles), those exhibiting a moderate fluorescent intensity are in the earliest stages of apoptosis (dashed green circles), and those that exhibit high propidium iodide and caspase fluorescence intensities report late apoptotic cells (dashed magenta circles). Using a contour plot of PI versus caspase-3/-7 intensity (Figure 5B), we were then able to create a cell-intensity differential plot and extract percentage occurrence on the basis of the number of cells within a specific state. The detected percentages are in excellent agreement with conventional controls for each sub-population (see Figures 5C and S15), confirming that our platform is able to rapidly and simultaneously analyze live, early, and late apoptotic cells through the extent of apoptosis and DNA content.

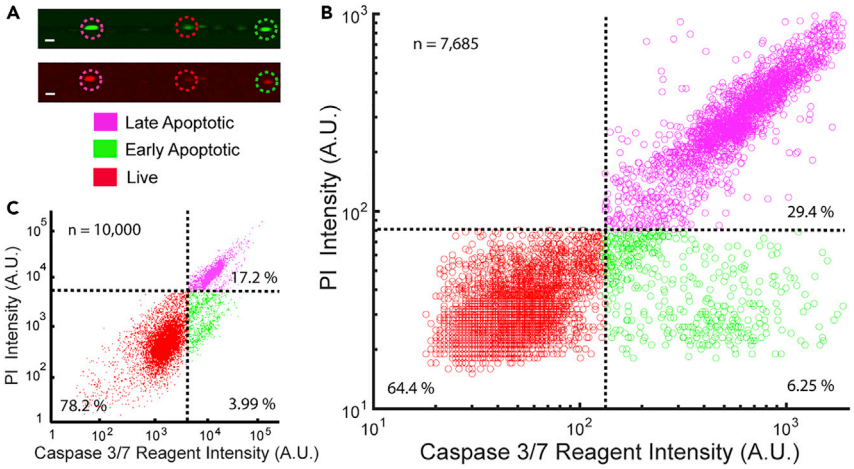

Figure 5. High-Throughput Detection of Apoptosis

(A) Images showing an illustrative example for each type of cell population: late apoptotic, early apoptotic, and live.

(B and C) Variation of fluorescence intensity of caspase-3/-7 reagent versus the membrane permeability indicator propidium iodide demonstrates agreement in the percentages of live, early apoptotic, and late apoptotic cells for the microfluidic imaging cytometer (B) and the commercial flow cytometer (C).

All scale bars represent 20 μm.

DISCUSSION

The imaging-based cytometry platform presented here allows for the detailed analysis of large numbers of cells and particles and has significant advantages over traditional point-based flow cytometry. First, when compared with conventional flow cytometry, adoption of the microfluidic format provides superior performance in terms of throughput while eliminating the need for system calibration using reference standards. Second, most conventional flow cytometers are incapable of resolving events that are separated by a distance smaller than the diameter of the focused laser beam. Third, maximum analysis rates from conventional methods are primarily determined by the stochastic nature of cellular arrival at the interrogation volume, which sets an upper limit to the concentrations of cells that can be assayed without generating unacceptably high numbers of coincidence events (assuming a Poisson distribution of particle arrival times). Using the current methodology, we are able to inertially position cells at small separations (even at high cell concentrations), significantly increasing analytical throughput. Moreover, because inertial focusing drives the positioning of cells, no sheath fluid is required, enabling operation at cell concentrations in excess of 35 million/mL. Such passive assembly of particles offers several advantages over conventional flow cytometry. Because excitation is bound to occur only in the focal volume, an increased number of cells will bypass the detection point leading to loss of real events and detection of false positives because of the increased probability of having of two or three cells concurrently traversing the detection volume.

The complexity of cellular interrogation and the need for large volumes of consumable (sheathing) reagents in conventional flow cytometer prevents the use of parallelization to enhance throughput and limits application in rare-event (cell) detection. Importantly, in the current approach, self-assembly of cells is a passive process governed by inertial forces, the concentration of the cell suspension under study, and the uniformity of the cell distribution within the device. The mammalian

HL60 cells used here have a diameter of approximately 15 μm. The underlying physics of self-assembly dictate that cells are packed in dense structures with a spacing roughly equal to twice the cell diameter.[17] Accordingly, such a spacing affords a limiting throughput of 96,000 cells/s. That said, the distribution of cells in the parallel microchannel network is not perfect and results in cells ordering in packed structures with some gaps. In the current work, this reduces throughput to between 50,000 and 60,000 cells/s. Regardless, such a throughput is more than an order of magnitude faster than any other microfluidic flow cytometer reported and is comparable with the limits of high-end, single-point flow cytometers. Further optimization of both the handling and distribution of the input cell suspension will almost certainly afford a significant increase in analytical throughput. In this regard, estimates of achievable throughputs for varying cell diameters are provided in Table S3. Typical mammalian cells range in size between 10 and 20 μm, which suggests a throughput of up to 180,000 cells/s for smaller cells (see Table S3 and Supplemental Experimental Procedures, Supplemental Note 3). In addition, the use of a high-power excitation source and a faster camera should allow blur-free quantitative phase, dark-field, and fluorescence imaging at flow speeds as high as 1 m/s.

As previously noted, the effective use of time-stretch imaging has been limited to particle or cell screening in high-speed flows where large differences in size and shape exist.[9] The microfluidic flow imaging cytometer demonstrated here achieves simultaneous fluorescence and bright-field detection at a throughput in excess of 25,000 cells/s by utilizing a massively parallel detection scheme with a far simpler optical configuration. Accordingly, one of the key advantages of our imaging cytometer over point-based detection schemes is the enormous enhancement in information content. Labeling heterogeneity, cellular size, the location of fluorescence organelles (such as the nucleus) in cellular structures, and morphological variations can all be extracted via fluorescence, bright-field (see Figure S16 and Supplemental Experimental Procedures, Supplemental Note 6), and dark-field measurements (see Figures S17 and S9C) on ultra-short timescales, which in turn provide novel insights into the size and shape of the nuclei that are critical in rapid disease diagnostics.[22] A direct refinement to the presented imaging platform would be the addition of 3D resolution.[23] Moreover, studies regarding the implementation of real-time image analysis for extracting scatterplots on the basis of fluorescence and dark-field intensities are currently underway. Finally, the described platform can be immediately applied to high-throughput and high-resolution analysis of a wide range of micrometer-sized objects such as polymer particles and beads in condensed-phase systems.[24,25] Given the aforementioned performance advantages over existing methods, we believe that the approach makes significant contributions to the large-scale screening of mammalian cells, provides detailed quantitative analyses of heterogeneous cell populations, and has the potential to allow rapid and systematic mapping of molecular interactions within real-world cell populations.

EXPERIMENTAL PROCEDURES

Microfluidic Device Fabrication

Microfluidic devices were fabricated by standard soft-lithographic techniques. The two-dimensional channel pattern was designed with AutoCAD (AutoCAD, 2014, Autodesk, USA) and printed onto a transparent film photomask (Micro Lithography Services, Chelmsford, UK). This photomask was subsequently used for patterning an SU-8 (MicroChem, Westborough, USA)-coated silicon wafer by conventional photolithography. A 10:1 mixture of polydimethoxysilane (PDMS) monomer and curing agent (Sylgard 184, Dow Corning, Midland, USA) was poured over the master

mold and peeled off after polymerization at 70°C for 4 hr. Inlet and outlet ports were punched with a hole puncher (Technical Innovations, West Palm Beach, USA), and the PDMS substrate was then bonded to a planar glass substrate (Menzel-Glaser, Braunschweig, Germany) after treating both surfaces in oxygen plasma (EMITECH K1000X, Quorum Technologies, East Sussex, UK) for 60 s.

Microfluidic Device Structure

A schematic of the microfluidic device is shown in Figure 1, and a CAD design is provided in Figure S1A. The first (inlet) zone acts to filter cell aggregates and particulates. The filtered cell suspension then enters a second zone where cells are inertially focused. Specifically, six parallel and winding channels are used to inertially focus cells to their equilibrium positions. These channels are 40 μm in width and 22 μm in height, and the curved geometry is designed to fix the ratio of lift forces to Dean forces at 0.1. The equilibrium cell or particle position for this configuration lies at the center of the long face of the channel. Such a configuration could cause cells and particles to be focused at the center of channel in the direction of flow, but at different locations in the z direction (along the height of the channel) because the long faces of the device are parallel to the imaging plane. This effect is minimized by constraining the height of the channel to 22 μm, which is comparable with the average cell size or particle size (12–17 μm). Each of the inertial focusing channels leads to an extended detection channel (R3 in Figure 1), which is switched back twice to provide three detection channels (per focusing channel) in the imaging region. Accordingly, the imaging region contains 18 parallel channels, each with a pitch of 20 μm and a length of 1,335 μm. This region exactly corresponds to the CMOS sensor area (1,335 × 1,335 μm) at 10× magnification.

Device Operation

The microfluidic device was placed on a motorized xy translation stage (Mad City Laboratories, Maddison, USA) mounted on an inverted microscope (Nikon Ti-E Microscope, Zurich, Switzerland). The cell (35 million cells/mL) suspension was loaded in a 1 mL syringe (Gastight Syringe, Hamilton Laboratory Products, NV, USA) and delivered at a flow rate of 150 μL/min with a precision syringe pump (Pump 11 Pico Plus, Harvard Apparatus, USA). Settling of cells within syringes was prevented by matching the density of the medium to the cell suspension with OptiPrep Density Gradient Medium (Sigma-Aldrich, Buchs, Switzerland). A commercial kit (DG06M, Bangs Labs, USA) consisting of five sub-populations of 8 μm polystyrene-based microspheres loaded with increasing amounts of Dragon Green fluorophore was used for intensity calibration measurements. The syringe was connected to the microfluidic device with syringe needles (GONANO Dosiertechnik GmbH, Germany) and Tygon tubing (Fisher Scientific, Reinach, Switzerland). Before use, channels were treated with FC Pluronic (Pluronic F127, Sigma-Aldrich, Buchs, Switzerland) in PBS 1× buffer solution (Invitrogen, Life Technologies, USA) for the prevention of cell adhesion to microchannel surfaces. A pre-filtering device (see Figure S1B) was used to prevent large cell clumps and cell debris from entering the flow cytometry microdevice. The maximum cell (or bead) density used was 3.5×10^7 cells/mL, and the longest experiment (at this cell density) was approximately 10 min. Over such a time period, we did not experience any problems with flow disruption or microchannel blockage; a uniform analysis rate of 50,000 cells/s was observed at all times.

Optical Setup and Data Acquisition

The optical system (see Figure S4A) consists of an inverted microscope (Eclipse Ti-E, Nikon, Zurich, Switzerland) equipped with a motorized stage (Mad City Labs,

Maddison, USA) and a dual-view detection system (Cairn Research, Kent, UK). The outputs of a red (640 nm; Coherent Cube, Glasgow, UK) and blue (488 nm; Coherent Sapphire, Glasgow, UK) laser were combined with a set of mirrors. After transmission through an acoustooptical tunable filter (AOTFnC-400-650-TN; AA Opto-electronic, Orsay, France) connected to an RF driver (AA Opto-electronic, Orsay, France), the combined beam was coupled with an optical fiber (QSMJ-3U3U-488-3.5/125-3AS-3,Oz Optics, Ottawa, ON, Canada) by means of an objective (20×, NA 0.4; Olympus, Thorlabs, Munich, Germany) mounted to a three-axis stage (Nanomax, Thorlabs, Munich, Germany). The fiber was then coupled to a Nikon TIRF illuminator that directed the laser beam into the microscope. Subsequently, the beam was reflected by a double dichroic mirror (zt 488/638 rpc; AHF, Tubingen, Germany) and focused into the microfluidic device with either a 10× objective (Plan Fluor 10×, NA 0.5; Nikon, Zurich, Switzerland) or a 20× (Plan Apo 20×, NA 0.45; Nikon, Zurich, Switzerland). Fluorescence originating from individual cells was then collected by the objective and passed through the dual-view filter box to provide images of all cells in the interrogated sample. Bright-field and dark-field imaging were accomplished in transmission mode with an LED light source (Spectra X; Lumencor, Beaverton, USA) and a bright-field (NA 0.5; Nikon, Zurich, Switzerland) and a dark-field (NA 0.6; Nikon, Zurich, Switzerland) condenser, respectively. The dual-view box was mounted between the objective lens and a CMOS camera (ORCA-flash 4.0; Hamamatsu, Solothurn, Switzerland) and comprised three mirrors, a dichroic filter, and two filters. For all experiments, a 640 DCXR (AHF, Tubingen, Germany) dichroic filter was used. For dual-color experiments, two emission filters D580/35 (AHF, Tubingen, Germany) and LP655 (AHF, Tubingen, Germany) were used to detect Alexa 488 and DRAQ5, respectively. For dark-field experiments, the red channel was used with a 593 LP emission filter. For bright-field experiments, the red channel was used without an emission filter. The two complete images (at two different wavelengths) were obtained simultaneously in different regions of the CMOS camera and in-house software (written in MicroManager 1.4.15, University of California, USA) was used to generate images and process data. Synchronization of both the laser and the LED light source with the camera was controlled with two ESIO AOTF controllers (ESImaging, Kent, UK). The AOTF and the LED were triggered by the CMOS camera with an 8-ms TTL pulse to achieve synchronization between the laser strobe and the LED with the exposure of the detector. The sampling frequency of the camera was 120 Hz, and the AOTF driver generated a pulse length that varied between 8 and 20 μs for both laser lines. For apoptosis experiments, the laser beam was transformed into a slit-shaped field, oriented along the microfluidic channel through the use of a cylindrical lens. With this excitation profile, only a narrow field needed to be illuminated, whereas traditional epi-illumination formats require that the entire objective field be illuminated. The light density provided by the cylindrical lens increased the effective illumination intensity by as much as one order of magnitude in comparison with normal, symmetric epi-illumination modalities. Fluorescence emitted by cells was collected by a 10× microscope objective (Plan Fluor 10×, NA 0.5; Nikon, Zurich, Switzerland) and passed through the dual-view filter box onto the CMOS camera.

Data Analysis

Post-processing of data was performed with algorithms that analyze fluorescence, dark-field, and bright-field images to extract the size, location, and intensity of cells. Generated contour plots contained data for each population or parameter (or combination) in a color-density layout format. Image analysis algorithms incorporated in MATLAB (MathWorks) allowed the accurate quantification of both cell size and fluorescence intensities (see Figure S18). Image acquisition (stored as a TIFF

stack) was analyzed for various cellular attributes, including cell area, cell size, and florescence intensity. Data obtained from the processing algorithm were then plotted as scatter density plots, scatterplots, and histograms. Initially, the image was read from the TIFF stack and a "de-noising" algorithm implemented in MATLAB for intensity-based filtering of noise from the image.[26] This step was important because it reduced background noise and made subsequent analysis less memory intensive. The inbuilt MATLAB function "imcontour" was then used to identify cell borders, and each of the cell images was stored as a closed contour. This closed contour provided cell-morphology parameters such as cell area, cell size, and centroid coordinates. With the cell-border information, the raw image was analyzed for fluorescence. The code searched for the maximum fluorescence intensity inside the defined cell area and also computed the mean florescence intensity of the cell.

Analysis of all images in a stack gave a data matrix containing information on the size, area, cell centroid, and fluorescence intensity of the cell. These raw data were then filtered for the removal of artifacts due to image noise and cell debris. The filtered data were then presented in the form of scatterplots and histograms. Coefficients of variation are defined as the ratio of the SD to the mean for a measured population. For apoptosis detection, the quadrant setting was determined on the basis of the position of the lowest density between the three sub-populations. Furthermore, by using the histograms of individual fluorescence channels, we were able to determine the intersection of two Gaussian populations.

For multi-parametric detection, it is essential to correlate co-localized events (for example, the cell periphery detected by Alexa 488 WGA must be correlated with the DRAQ5 nuclear stain). This was achieved with information derived from the coordinates of the centroid of the detected event. First, data obtained from different detection channels were corrected for offsets in the position of detected events in the image. Subsequently, images from both channels were analyzed for cell attributes. Detected events were then correlated by comparison of the coordinates of the detected events in both channels. Once the events were correlated, scatterplots of chosen attributes could be generated.

Cell Culture

Experiments were performed on four different cell lines: HL-60 (Sigma-Aldrich, Switzerland), JURKAT Clone E6-1 (ATCC, USA), HeLa (ATCC, USA), and K-562 (ATCC, USA). All cell lines were initially tested for mycoplasma contamination and then cultured in RPMI-1640 medium (Life Technologies, Switzerland) supplemented with 10% (v/v) fetal bovine serum (FBS) (Life Technologies, Switzerland) and 1% (v/v) penicillin-streptomycin (10,000 U/mL; Life Technologies, Switzerland) in a CO_2 incubator (New Brunswick Galaxy 170 S, Switzerland) at +37°C, 5% CO_2. For apoptosis experiments, cells were cultured under the same conditions as mentioned previously. For cell-cycle control experiments, the FBS concentration was reduced from 10% to 0.5%. Cells were split every 2 days to maintain a concentration of 2×10^5 viable cells/mL. All experiments were performed on cells in the exponential (log) phase of growth.

Viability Tests

Cell viability was evaluated with a trypan blue (Life Technologies, Switzerland) exclusion assay according to standard protocols (Lonza, Switzerland). The cell sample was diluted in trypan blue (1:1 ratio) and incubated for 2 min. Ten microliters of the sample was then transferred into a hemocytometer chamber (Neubauer Improved, Karl Hecht "Assistent" GmbH, Germany), and cells were counted under

a microscope in four 1 × 1 mm squares for determining the average number of cells per square. Viable cells (viability 97% ± 2%) remain unstained and non-viable turn blue.

Cell Fixation and Staining for High-Throughput and Multi-color Experiments

For actin staining, HL60 cells were fixed in 4% paraformaldehyde at 37°C for 30 min. After fixation, the cells were rinsed by PBS and permeabilized for 30 min in PBST (0.1% Triton X in PBS). The permeabilized cells were blocked with 1% BSA in PBST for 4 hr at 4°C and incubated with Alexa Fluor 488 WGA (1:200, A12379; Life Technologies) for 1 hr at room temperature. After being rinsed in PBST, cells were stored in PBS at 4°C. For multi-color experiments, the cell nucleus was stained with DRAQ5 fluorescent dye (Thermo Scientific).

HL-60 and HeLa Cell-Cycle Control

HL-60 and HeLa cell cycles were arrested in the G2/M stage by incubation for 16 hr with nocodazole (50 ng/mL; Sigma-Aldrich, Switzerland) in the cell-culturing conditions described but were supplemented with 0.5% (v/v) FBS and 1% (v/v) penicillin-streptomycin (10,000 U/mL) in a CO_2 incubator (New Brunswick Galaxy 170 S, Switzerland) at +37°C, 5% CO_2,. The cell cycle was stopped in the G1 stage after incubation for 3 hr with mitomycin C (10 μg/mL; Sigma-Aldrich, Switzerland) under the same conditions as for the nocodazole treatment. Drug-treated cells were washed with DPBS (Life Technologies, Switzerland) and fixed by dripping 70% ethanol (at −20°C). In brief, fixed cells were vortexed for 30 s, incubated at −20°C for 1 hr, and then washed twice with DPBS and once with deionized water. Washed cells were incubated on ice for 15 min with SYTOX green nucleic acid stain (1 μM; Life Technologies, Switzerland). In the next step, cells were concentrated (100 × *g*, 5 min), resuspended in 10 mL of deionized water, and filtered through a 40 μm cell strainer (Fisher Scientific) to avoid cell clumps. Cells were then collected, concentrated, and resuspended in deionized water with 36% OptiPrep Density Gradient Medium (Sigma-Aldrich, Switzerland). For experiments performed in the imaging flow cytometry platform and the Fortessa commercial flow cytometer (BD Biosciences, Switzerland), 30 million cells/mL and 10^6 cells/mL were used, respectively.

Induction of Apoptosis and Cell Staining

Apoptosis in Jurkat cells was induced by a standard protocol (Immuno Chemistry Technologies). Cells were treated with 12 μM (S)-(+)-camptothecin (Sigma-Aldrich, Switzerland) for 5 hr, causing an inhibition of topoisomerase that in turn resulted in S-phase cell apoptosis. Drug treatment was terminated by centrifuging (100 × *g*, 5 min) and washing cells twice with DPBS (Life Technologies, Switzerland). For apoptotic cell analysis, CellEvent Caspase-3/7 Green Detection Reagent (Life Technologies, Switzerland) was used as a fluorogenic substrate for activated caspase-3/-7. Washed cells were resuspended in complete RPMI-1640 medium and incubated with 8 μM CellEvent Caspase-3/7 Green Detection Reagent for 30 min and propidium iodide (3 μg/mL final concentration; Sigma-Aldrich, Switzerland) for 15 min at 37°C. After incubation, cells were concentrated (100 × *g*, 5 min), the supernatant was discarded (to minimize the background), and the cells were resuspended in complete RPMI-1640 medium with 20% OptiPrep.

Flow Cytometry and Analysis

A maximum of 400 events/s were measured for each sample in a Fortessa flow cytometer (BD Biosciences, San Jose, CA). Data were analyzed with CellQuest 3.3 (BD Biosciences, San Jose, CA). A plot of forward scatter against side scatter was first used for gating

cellular events and eliminating events caused by cell debris. Subsequently, each fluorescence detection channel was used to eliminate cell aggregates and gate single-cell events. A plot of peak area against the peak height for the given fluorescent detection channel was used for gating single cells. Finally, resulting scatterplots of the relevant parameters were created for each cell population. The number of gated events corresponds to 20,000 events for statistical robustness in data analysis.

SUPPLEMENTAL INFORMATION

Supplemental Information includes Supplemental Experimental Procedures, 18 figures, and 3 tables and can be found with this article online at http://dx.doi.org/10.1016/j.chempr.2017.08.005.

AUTHOR CONTRIBUTIONS

S.S, R.A., and A.dM. conceived the project, devised the research plan, developed the setup and methodology, and performed the experiments. R.A. performed image processing. J.R. developed cell protocols and cultured and stained the biological samples. S.S., R.A., and A.dM. wrote the manuscript.

ACKNOWLEDGMENTS

The authors would like to acknowledge ETH Zürich and the National Research Foundation of Korea (Global Research Laboratory Program grant K20904000004-10A0500-00410) for partial support. The authors would like to thank Mr. Yun Ding for help with the preparation of the figures.

Received: June 12, 2017
Revised: July 17, 2017
Accepted: August 16, 2017
Published: October 12, 2017

REFERENCES

1. Hasegawa, D., Bugarin, C., Giordan, M., Bresolin, S., Longoni, D., Micalizzi, C., Ramenghi, U., Bertaina, A., Basso, G., Locatelli, F., et al. (2013). Validation of flow cytometric phospho-STAT5 as a diagnostic tool for juvenile myelomonocytic leukemia. Blood Cancer J. *3*, e160.

2. Sandberg, J., Werne, B., Dessing, M., and Lundeberg, J. (2011). Rapid flow-sorting to simultaneously resolve multiplex massively parallel sequencing products. Sci. Rep. *1*, 108.

3. De Rosa, S.C., Herzenberg, L.A., Herzenberg, L.A., and Roederer, M. (2001). 11-color, 13-parameter flow cytometry: identification of human naive T cells by phenotype, function, and T-cell receptor diversity. Nat. Med. *7*, 245–248.

4. Gross, H.J., Verwer, B., Houck, D., and Recktenwald, D. (1993). Detection of rare cells at a frequency of one per million by flow cytometry. Cytometry *14*, 519–526.

5. Nebe-von-Caron, G., Stephens, P.J., Hewitt, C.J., Powell, J.R., and Badley, R.A. (2000). Analysis of bacterial function by multi-colour fluorescence flow cytometry and single cell sorting. J. Microbiol. Methods *42*, 97–114.

6. Mao, X., Lin, S.C., Dong, C., and Huang, T.J. (2009). Single-layer planar on-chip flow cytometer using microfluidic drifting based three-dimensional (3D) hydrodynamic focusing. Lab Chip *9*, 1583–1589.

7. Golden, J.P., Kim, J.S., Erickson, J.S., Hilliard, L.R., Howell, P.B., Anderson, G.P., Nasir, M., and Ligler, F.S. (2009). Multi-wavelength microflow cytometer using groove-generated sheath flow. Lab Chip *9*, 1942–1950.

8. Spencer, D., Elliott, G., and Morgan, H. (2014). A sheath-less combined optical and impedance micro-cytometer. Lab Chip *14*, 3064–3073.

9. Goda, K., Ayazi, A., Gossett, D.R., Sadasivam, J., Lonappan, C.K., Sollier, E., Fard, A.M., Hur, S.C., Adam, J., Murray, C., et al. (2012). High-throughput single-microparticle imaging flow analyzer. Proc. Natl. Acad. Sci. USA *109*, 11630–11635.

10. Hur, S.C., Tse, H.T., and Di Carlo, D. (2010). Sheathless inertial cell ordering for extreme throughput flow cytometry. Lab Chip *10*, 274–280.

11. Schonbrun, E., Gorthi, S.S., and Schaak, D. (2012). Microfabricated multiple field of view imaging flow cytometry. Lab Chip *12*, 268–273.

12. McKenna, B.K., Evans, J.G., Cheung, M.C., and Ehrlich, D.J. (2011). A parallel microfluidic flow cytometer for high-content screening. Nat. Methods *8*, 401–403.

13. Diebold, E.D., Buckley, B., Gossett, D.R., and Jalali, B. (2013). Digitally synthesized beat frequency multiplexing for sub-millisecond fluorescence microscopy. Nat. Photon. *7*, 806–810.

14. George, T.C., Fanning, S.L., Fitzgerald-Bocarsly, P., Medeiros, R.B., Highfill, S., Shimizu, Y., Hall, B.E., Frost, K., Basiji, D., Ortyn, W.E., et al. (2006). Quantitative measurement of nuclear translocation events using similarity analysis of multispectral cellular images obtained in flow. J. Immunol. Methods *311*, 117–129.

15. Hess, D., Rane, A., deMello, A.J., and Stavrakis, S. (2015). High-throughput, quantitative enzyme kinetic analysis in microdroplets using stroboscopic epifluorescence imaging. Anal. Chem. *87*, 4965–4972.

16. Di Carlo, D., Irimia, D., Tompkins, R.G., and Toner, M. (2007). Continuous inertial focusing, ordering, and separation of particles in microchannels. Proc. Natl. Acad. Sci. USA *104*, 18892–18897.

17. Di Carlo, D., Edd, J.F., Humphry, K.J., Stone, H.A., and Toner, M. (2009). Particle segregation and dynamics in confined flows. Phys. Rev. Lett. *102*, 094503.

18. Edd, J.F., Di Carlo, D., Humphry, K.J., Köster, S., Irimia, D., Weitz, D.A., and Toner, M. (2008). Controlled encapsulation of single-cells into monodisperse picolitre drops. Lab Chip *8*, 1262–1264.

19. Dapena, C., Bravo, I., Cuadrado, A., and Figueroa, R.I. (2015). Nuclear and cell morphological changes during the cell cycle and growth of the toxic dinoflagellate *Alexandrium minutum*. Protist *166*, 146–160.

20. Ormerod, M.G., Titley, J.C., and Imrie, P.R. (1995). Use of light scatter when recording a DNA histogram from paraffin-embedded tissue. Cytometry *21*, 294–299.

21. Wlodkowic, D., Khoshmanesh, K., Sharpe, J.C., Darzynkiewicz, Z., and Cooper, J.M. (2011). Apoptosis goes on a chip: advances in the microfluidic analysis of programmed cell death. Anal. Chem. *83*, 6439–6446.

22. Zwerger, M., Ho, C.Y., and Lammerding, J. (2011). Nuclear mechanics in disease. Annu. Rev. Biomed. Eng. *13*, 397–428.

23. Liu, S., and Hua, H. (2011). Extended depth-of-field microscopic imaging with a variable focus microscope objective. Opt. Express *19*, 353–362.

24. Tang, H., Deschner, R., Allen, P., Cho, Y., Sermas, P., Maurer, A., Ellington, A.D., and Willson, C.G. (2012). Analysis of DNA-guided self-assembly of microspheres using imaging flow cytometry. J. Am. Chem. Soc. *134*, 15245–15248.

25. Deschner, R., Tang, H., Allen, P., Hall, C., Hlis, R., Ellington, A., and Willson, C.G. (2014). Progress report on the generation of polyfunctional microscale particles for programmed self-assembly. Chem. Mater. *26*, 1457–1462.

26. Crocker, J.C., and Grier, D.G. (1996). Methods of digital video microscopy for colloidal studies. J. Colloid Interface Sci. *179*, 298–310.